International Journal of Thermophysics, Vol. 28, No. 5, October 2007 (© 2007)
DOI: 10.1007/s10765-006-0145-z

Determination of the Anisotropic Thermal Conductivity of a Carbon Aerogel–Fiber Composite by a Non-contact Thermographic Technique[1]

V. Drach,[2,3] M. Wiener,[4] G. Reichenauer,[4] H.-P. Ebert,[2] and J. Fricke[4]

The carbon-composite under investigation consists of a felt of carbon fibers infiltrated by a nanoporous sol-gel derived carbon aerogel; in addition, cracks caused by the shrinkage of the gel upon drying are present within the composite. Due to the anisotropic structure of the felt, consisting of a pinned stack of fiber mats, the thermal conductivity of the compound is anisotropic. The components of the thermal conductivity in the different directions were measured at room temperature using a non-contact technique, which was formerly established for fibers and foils. Here, a high-power laser diode is used for non-contact heating and a thermographic system for non-contact detection of the surface temperature of the samples. The stationary profile of the surface temperature next to the laser focus was evaluated with respect to the lateral thermal conductivity. Using a line-shaped laser focus, a one-dimensional heat flow within the samples was established and the two relevant components of the thermal conductivity in the different directions could be separated by investigating slices of the composite with different orientation to the main fiber orientation of the felt. The anisotropy of the thermal conductivity, i.e., the ratio of the components perpendicular and parallel to the felt surface, was determined to be about two under vacuum conditions. This relatively small thermal anisotropy was in qualitative agreement with preliminary tests of the electrical conductivity. In addition, local inhomogeneities due to macroscopic voids within the samples influenced the observed temperature profile. As alternative measurement variants, point-shaped laser-heatingof sample discs was used and evaluated in terms of a two-dimensional

[1]Paper presented at the Seventeenth European Conference on Thermophysical Properties, September 5–8, 2005, Bratislava, Slovak Republic.

[2]Bavarian Center for Applied Energy Research, ZAE Bayeru, Am Hubland, 97074 Würzburg, Germany.
[3]To whom correspondence should be addressed. E-mail: drach@zae.uni-wuerzburg.de
[4]Physics Department, University of Würzburg, Am Hubland, 97074 Würzburg, Germany.

heat flow and periodic, i.e., dynamical heating of the sample slices with a line-shaped laser focus was used. The reliability of the results was also tested by comparing them to data derived with a guarded-hot-plate measurement of a (1.1 × 15 × 15) cm^3 large tile.

KEY WORDS: aerogel; anisotropy; carbon; thermal conductivity; thermography.

1. INTRODUCTION

Nanoporous carbon aerogels and composites based on them are of interest for high temperature applications such as insulation materials, or as functional materials in filters or catalysts. The composite consists of a felt of carbon fibers, infiltrated by a nanoporous carbon aerogel. The synthesis of the latter starts with a solution of resorcinol (R), formaldehyde (F), catalyst, and water. Gelation of the solution and aging provide the nanostructured network. The solvent (water) in the pores is replaced by acetone and the gel is (subcritically) dried. The resulting RF-aerogel can be converted into a pure carbon-aerogel by pyrolysis [1]. The pore sizes within the carbon-aerogel can be tailored to be in the range of several tens of nanometers up to several micrometers, depending on the processing parameters [2]. The nanoporous carbonaceous structure of the aerogel reduces gaseous thermal conduction as well as radiative thermal transport. Thus, its potential use as an insulation material is obvious [3].

In order to improve the mechanical stability of the carbon-material, the formation of the RF-aerogel is performed within a carbon-felt as a matrix. The latter is a felt consisting of a pinned stack of fiber mats (see Fig. 1). The pinning fibers are bundles of long fibers and are a substantial portion of the whole amount of fibers. Cracks of up to about 0.5 mm in size (visually estimated) arise within the aerogel phase, caused by the shrinkage of the gel upon drying, with the fiber matrix acting as a stiff skeleton. While the density of the carbon-fiber felt is about 100 $kg \cdot m^{-3}$, the density of the investigated composite is about 230 $kg \cdot m^{-3}$. Due to the anisotropic structure of the felt, the thermal conductivity of the compound is also anisotropic, i.e., a higher thermal conductivity within the plane of the fiber mats occurs. It was the aim of the present investigation to determine the components of the anisotropic thermal conductivity of this composite material.

Due to the inhomogeneities, i.e., the cracks of up to about 0.5 mm in size and the correspondingly rough sample surface, a standard laser-flash experiment [4] appeared to not be suitable for this task. On the other hand, non-contact methods such as the laser-flash technique or photothermal techniques have the advantage of simplicity in sample preparation and

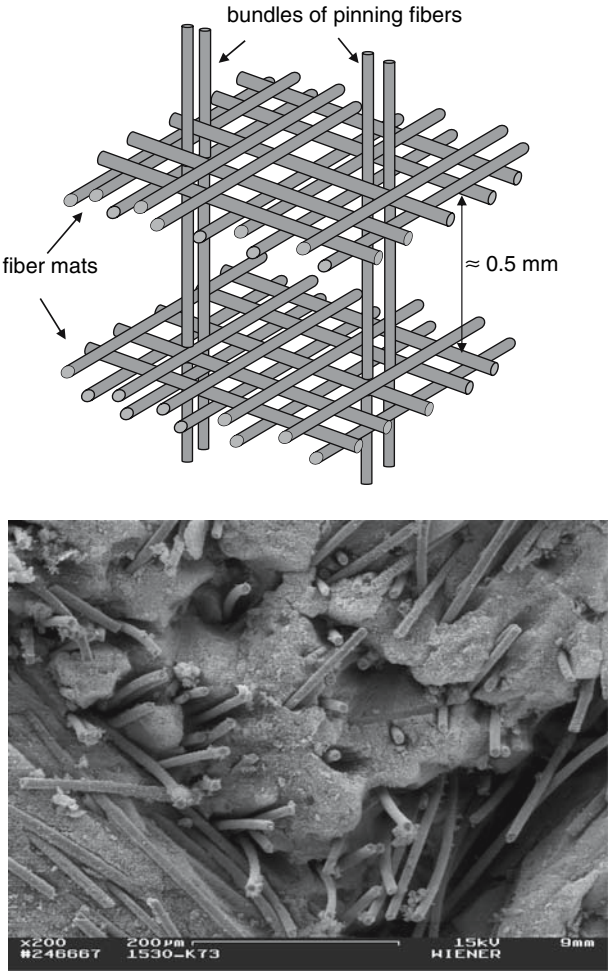

Fig. 1. Schematic diagram of the fiber arrangement in the carbon-fiber felt (top) and REM-picture of the investigated material with carbon-aerogel incorporated (bottom). In detail, the pinning fibers are bundles of long fibers, which intersect the fiber mats. The orientation of the fiber mats is not obvious in the SEM-image due to the inspection at a point of fracture.

the lack of disturbing sensor/heating elements [5–7]. The use of non-contact temperature detection by infrared detectors also allows the investigation of thermal anisotropy for plastic foils [8]. Here, a fully non-contact technique was used, which was formerly applied for the thermal characterization of a variety of small sample systems [9,10]. With the availability

of high-performance thermography systems [11], there is enough flexibility to perform non-contact measurement techniques in thermal analysis. In principle, many experimental modifications can be realized by changing the geometry of the heating source (point-like, line-wise, or plane), the type of temporal evolution (stepwise, periodical, or stationary) and the method of temperature measurement (spatial and/or temporal, backside, or front-side) (see, e.g., Refs. 12 and 13). The present article demonstrates the application of the non-contact measurement technique for the thermal analysis of an anisotropic carbon-fiber-felt system.

2. EXPERIMENTAL SETUP

The main feature of the experimental setup is a thermography system, which acts as a non-contact detector for the spatial variation in temperature of the sample (see Fig. 2). Therefore, we use the acronym "Thermoscan" for this technique. In the setup in question, local (line-wise or point-like) continuous heating of the sample is provided by the absorption of the (visible) beam of a high-power laser diode. The laser-diode emission is mainly divergent in the vertical direction. The beam profile on the sample surface is defined by slits, lenses, and mirrors to achieve line-wise or point-like heating of the sample. After the stationary state is achieved, the temperature distribution on both sides of the laser-heated region is detected by a thermography system and used for further evaluation.

The thermography system is an AEGAIS-system from AIM, Heilbronn, Germany, with a PtSi-based focal plane array of 256×256 pixels. It is sensitive to wavelengths between 2 and $5\,\mu$m and has a resolution (NETD = noise equivalent temperature difference) of about 0.07 K in a typical configuration at 300 K. For the case of stationary conditions, pictures are taken by averaging thermal emission over about 2 s. For evaluation, a zero picture without laser heating was subtracted in order to extract the temperature increase and to optimize spatial homogeneity.

Periodic heating was realized by controlling the output of the laser diode with the voltage of a frequency generator. The temporal evolution of the temperature on the sample surface was recorded by use of the (smaller) 128×128 pixel subframe of the thermography system and acquisition of a series of 126 pictures.

The sample is placed within a vacuum chamber in order to eliminate convection and to render gaseous conductive heat transfer negligible compared to the radiative heat transfer from the sample surface. The vacuum chamber contains a glass entrance window for the laser beam and a calcium fluoride (CaF_2) window for observing the sample with the infrared system. With the sample surface being black in the visible and infrared

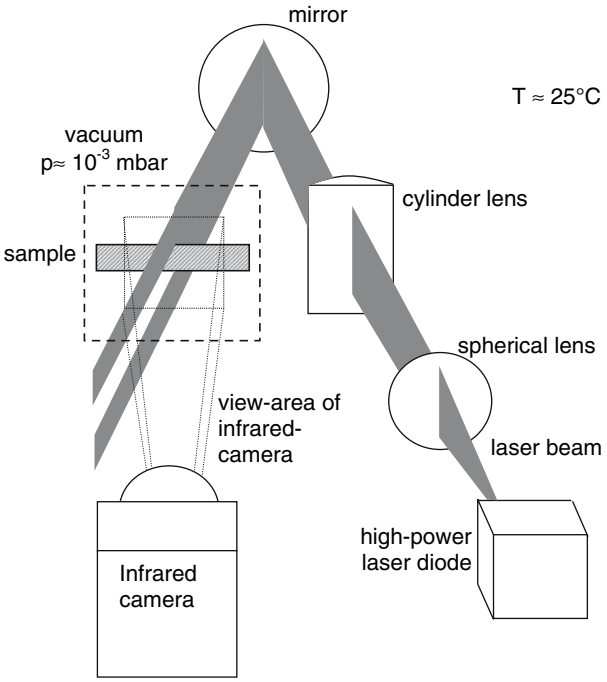

Fig. 2. Schematic of the experimental setup called "Thermoscan".

spectrum, no additional coating was necessary to improve the absorption of the impinging laser light and the emission of thermal radiation. The measurement principle is based on the detection of a stationary temperature profile.

The samples were prepared as slices of about 1.5-mm thickness, which were cut from a larger cylindrical body either along the main fiber orientation, i.e., of the fiber-mat, or perpendicular to the fiber orientation. Both disc-shape and plate-shape samples were prepared and used for different measurement variants (see Fig. 3). The size of the plate samples was about $(21 \times 43)\,\mathrm{mm}^2$; the diameter of the disc samples was about 24 mm.

3. STATIONARY LINE-SHAPED LASER-HEATING

3.1. Analytical Treatment

The detected temperature increase along the sample surface is evaluated under stationary conditions. When using the line-wise laser focus

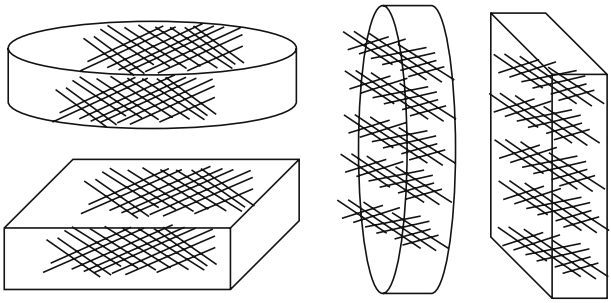

Fig. 3. Illustration of the prepared sample slices: Left: disc- and plate-shaped samples, whose fiber orientation is parallel to the slice plane; right: perpendicular case. The orientation of the fiber mat is schematically indicated.

(focal line extending along the z-axis, see Fig. 4), heat transport along the sample is mainly one-dimensional. With this assumption, the stationary temperature distribution can be derived in analogy to a thin rectangular fin, which is partly fixed to a surface of given temperature and cooled by radiation (and convection) from its free surface. The following relation holds for the freestanding part of the sample [14]:

$$\Delta T(x) = \Delta T_0 \frac{\cosh[(L-x)/l_0]}{\cosh[L/l_0]} \xrightarrow{l_0 \ll L} \Delta T_0 \exp\left(-\frac{|x|}{l_0}\right). \tag{1}$$

Here, ΔT_0 denotes the (maximum) temperature increase within the focus line of the laser beam at $x = 0$. L denotes the free-standing length measured from the focus line (see Fig. 4). The quantity l_0 is the characteristic decay length, which depends on the lateral thermal conductivity λ the thickness D of the sample, and the heat transfer coefficient α from the sample surface to the surrounding area;

$$l_0 = \sqrt{\frac{\lambda D}{2\alpha}}. \tag{2}$$

This decay length l_0 is a measure of the spatial variation of the temperature and does not depend on the absolute value of the temperature increase. For small decay lengths, the edge effect due to the finite sample length L can be neglected and the approximation on the right-hand side of Eq. (1) can be used.

The heat transfer coefficient α is solely determined by radiative heat transfer. Assuming the surrounding surfaces to be black, the radiative heat transfer coefficient can be calculated using the linearized Stefan-Boltzmann law at the sample temperature ($T = 300\,\mathrm{K}$);

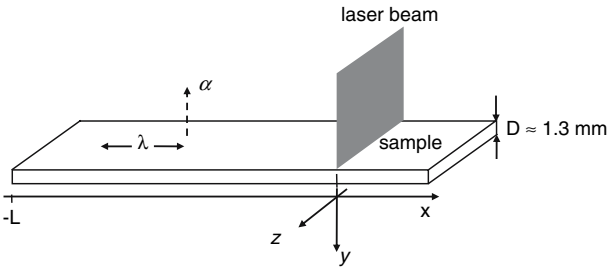

Fig. 4. Schematic diagram of the plate-like sample and the line-shaped laser beam including the relevant geometrical and thermophysical parameters.

$$\alpha = 4\sigma\,\varepsilon\,T^3. \tag{3}$$

with the Stefan-Boltzmann constant σ. The emissivity ε of the sample surface was determined separately from spectroscopic measurements of the infrared properties of the sample surface and appropriate Planck-weighting. Samples with different fiber orientation were characterized and the dependence on the fiber orientation was found to be negligible, resulting in a value $\varepsilon(300\,\mathrm{K}) = 0.93 \pm 0.03$.

3.2. Numerical Simulation

The assumption of purely one-dimensional heat transport involves the assumption that the temperature gradients in the y-direction are negligible compared to the gradients in the x-direction, i.e., a perfect perpendicular penetration of heat despite the laser surface heating. The validity of this assumption has to be tested, when relatively thick samples or highly anisotropic samples are under investigation. This was done by use of numerical simulations by the software HEAT2 [16] for the experimental conditions given here. The geometry, the boundary conditions, and the stationary temperature distribution of a sample cross-section as derived via simulations are depicted in Fig. 5. While the simulations have identical geometry and boundary conditions, they differ in the orientation of the fibers with a chosen reasonable thermal conductivity of $\lambda_{II} = 0.8\,\mathrm{W{\cdot}m^{-1}{\cdot}K^{-1}}$ parallel to the fiber orientation and $\lambda_{\perp} = 0.4\,\mathrm{W{\cdot}m^{-1}{\cdot}K^{-1}}$ perpendicular to the fiber orientation. The simulation is two-dimensional, i.e., it is valid for an infinite sample extending in the z-direction perpendicular to the plane shown.

The temperature distribution exhibits a distortion next to the focus, especially in the case of the parallel fiber orientation, since heat is

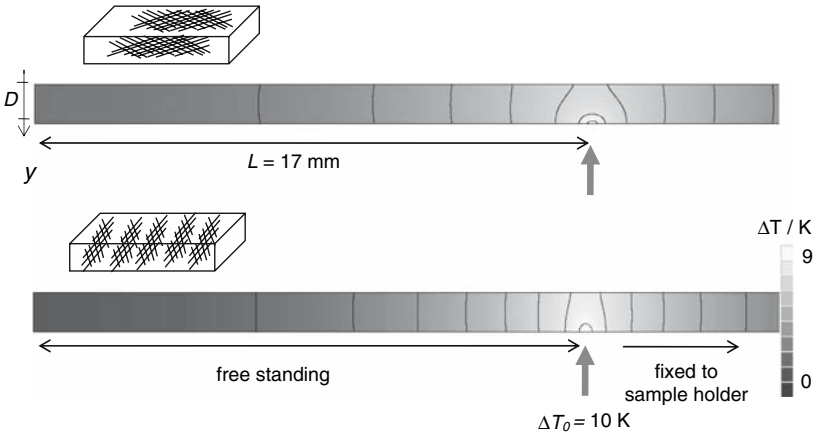

Fig. 5. Simulated 2D-result for the cross-section of a free standing plate sample with the main fiber orientation parallel (upper part) and perpendicular (lower part) to the plate surface, i.e., the surface of detection (see also Fig. 4). The geometrical setup is representative of the experiments described, the thickness of the samples is $D = 1.25$ mm. The boundary conditions are the maximum temperature increase ΔT_0, the location of the laser focus, a (position independent) heat transfer coefficient of $\alpha = 5.7\,\mathrm{W{\cdot}m^{-2}{\cdot}K^{-1}}$ and a fixed temperature $\Delta T = 0$ at the sample holder ($x = 17$ mm). The stationary temperature distribution is visualized by the gray scale and the isotherms, which are separated by 1 K.

transported mainly laterally. The distortion due to superficial laser heating is also reflected in the corresponding surface temperature profiles (see Fig. 6), which differ for the surface of laser impingement and the opposite side in the vicinity of the focus. Due to the non-isotropic thermal conductivity, the temperature decay differs for the two fiber orientations, i.e., the outer temperature $\Delta T(x = -L)$ differs. As expected, the assumption of one-dimensional heat transfer, which is characterized by vertical isotherms, is best fulfilled for the perpendicular fiber orientation. Here, the best agreement with the analytical correlation (Eq. 1) is obtained. Deviations arise from the multi-dimensional effects next to the laser surface heating and the additional heat losses at the end of the sample strip. As a result, the analytical correlation appears to be applicable in the lateral region, which is not too close to the focus and not too close to the edge, i.e., in a range of about $-0.012 < x/m < -0.002$. Deviations between simulation and analytical correlation within the right branch of the sample, which is fixed to the sample holder, are stronger due to the different boundary conditions, but are not relevant for further evaluations.

3.3. Experimental Results

In Fig. 7, the experimental results for two sample plates with different fiber orientations are shown. Obviously, a steeper temperature gradient illustrates the lower thermal conductivity for the case of perpendicular fiber orientation. This is accompanied by a higher maximum temperature at the focus location, since laser power is identical for the two measurements shown. The temperature profiles are extracted within an appropriate sample region and compared with the analytical correlation (Eq. 1). From the fit, the decay length (l_0) is obtained, yielding the unknown thermal conductivity λ according to Eq. (2). An additional fit quantity is the maximum temperature increase ΔT_0. The latter depends on the laser power, which was also varied for consistency checks, since the decay length (l_0) must be independent of the applied ΔT_0 as long as the temperature dependence of λ can be neglected.

For the thermal conductivity parallel and perpendicular to the fiber orientation the values of $\lambda_{\text{II}} = (0.76 \pm 0.05)\,\text{W}\cdot\text{m}^{-1}\cdot\text{K}^{-1}$ and $\lambda_{\perp} = (0.40 \pm 0.03)\,\text{W}\cdot\text{m}^{-1}\cdot\text{K}^{-1}$ were obtained. The uncertainty in the thermal conductivity results from the uncertainty in the heat transfer coefficient α (overall relative uncertainty 5%) and from the uncertainty in the decay length ($\Delta l_0 \approx \pm\ 0.1\,\text{mm}$), which is due to uncompensated temperature inhomogeneities and scatter within the fit. Additionally, an uncertainty in the free-standing length ($\Delta L \approx \pm\ 0.5\,\text{mm}$) arises from the geometrically imperfect sample positioning which affects l_0. Furthermore, the uncertainty for the sample thickness ($d = 1.30\,\text{mm}$ or $1.25\,\text{mm}$) was assumed to be $\Delta d \approx \pm\ 20\,\mu\text{m}$. The overall uncertainty in λ, computed by error propagation of these uncertainty sources, coincides with the scatter of different single measurement points.

For the sample with perpendicular fiber orientation, voids were visible in some parts of the samples. While for the measurements shown in Fig. 7, these voids were not situated in the evaluated region on the left side of the focus; they become thermally important when the fixation of the sample is reversed. Corresponding results are shown in Fig. 8, which can be directly compared to the left side of Fig. 7. A steeper temperature slope is obtained in the region of the voids, corresponding to a locally reduced thermal conductivity. An effective value of the lateral thermal conductivity is computed by fitting Eq. (1) to the whole temperature profile, resulting in $\lambda_{\perp} \approx 0.2\,\text{W}\cdot\text{m}^{-1}\cdot\text{K}^{-1}$, which is about half the value for the homogeneous region. This effective value is only a estimation for the lower limit, since the sample thickness is in the order of the void size and does not represent mean sample properties. Additionally, sample inhomogenieties became visible as local variations of the maximum temperature within the focal line

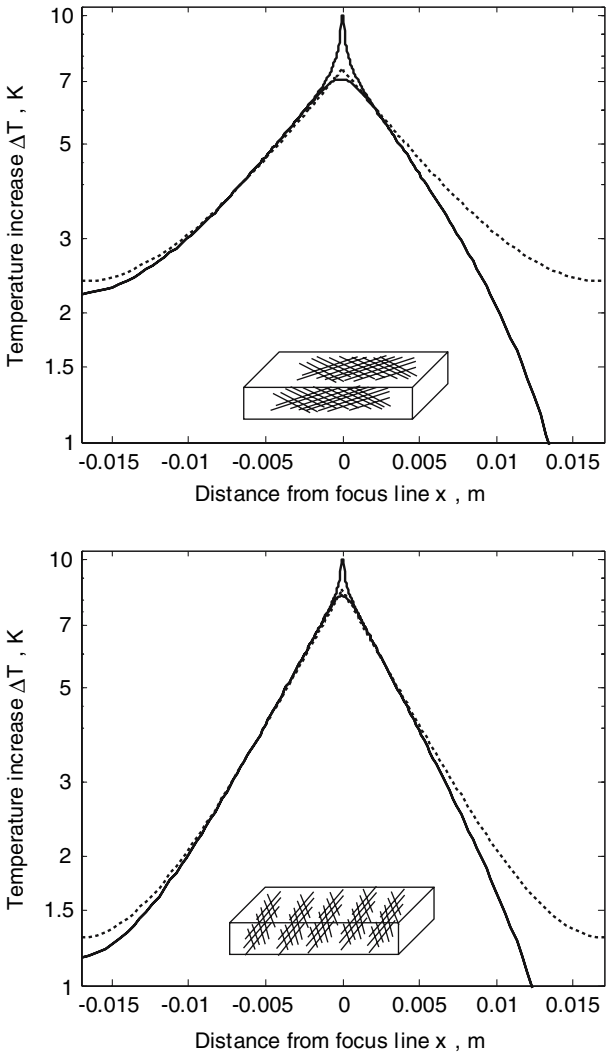

Fig. 6. Temperature profiles derived from simulations according to Fig. 5 for the parallel fiber orientation (upper part) and the perpendicular orientation (lower part). Full lines depict the simulated temperature at the upper and lower sample surfaces; the two branches differ only in the focus region ($x = 0$); the largest ΔT belongs to the surface of laser impingement, the somewhat smaller ΔT belongs to the opposite surface. Dotted line is the corresponding analytical solution (Eq. 1) for the one-dimensional case.

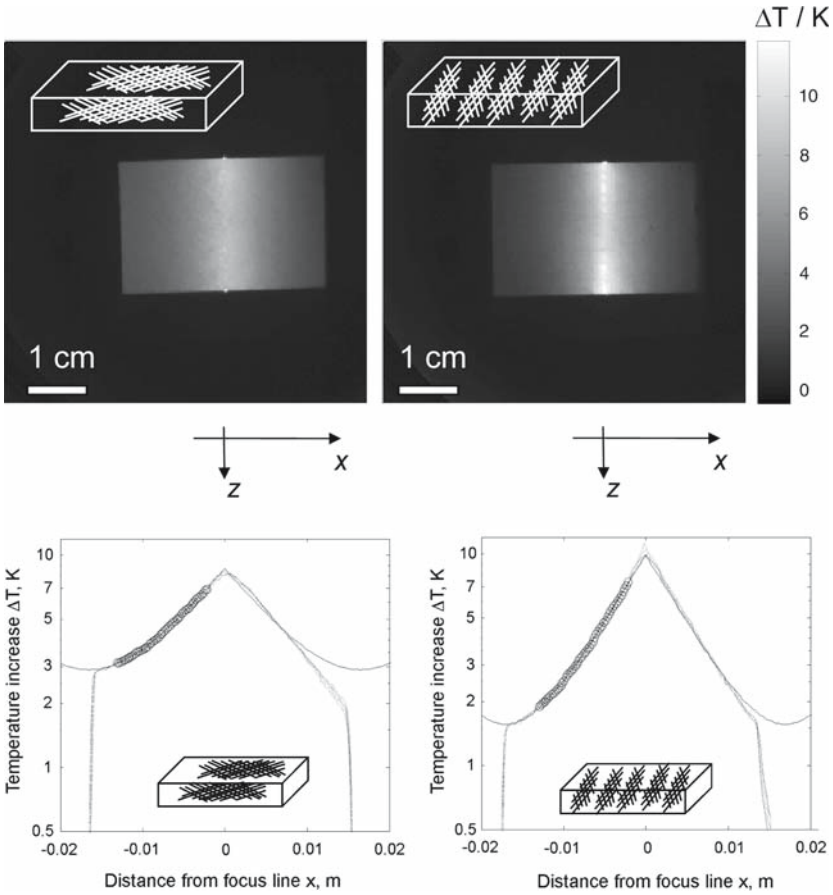

Fig. 7. Measurement results for line-wise, stationary laser heating ($P = 400\,\text{mW}$) of a sample plate with parallel fiber orientation (left) and perpendicular fiber orientation (right). In the upper part the thermography pictures of the sample surface opposite to the incident laser focus line are shown. In the lower part, semi-logarithmic plots of the temperature profiles are depicted: single scan data extracted from the thermography are shown as dashes. Averaged data are depicted as cycles on the free-standing side $x < 0$. The fit to Eq. (1), which is valid for $|x| < L = 0.0017\,\text{m}$, is shown as full line.

of the laser (see Fig. 7 top right). No inhomogeneity was detected for the sample with parallel fiber orientation, where the distance of fibers within the mats is much smaller than the distance between the fiber mats (see Fig. 1).

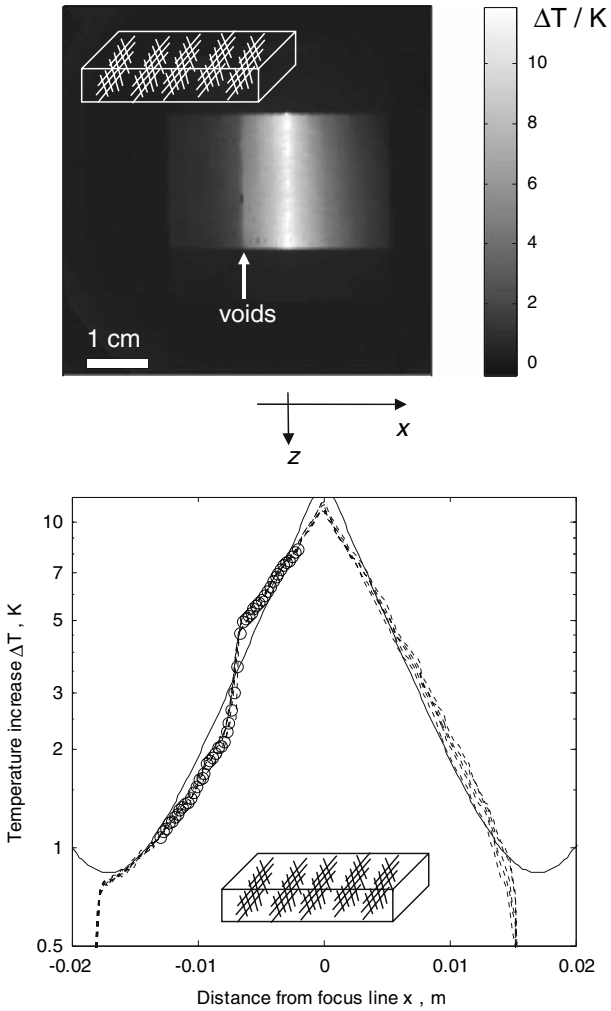

Fig. 8. Results for a region with a visible sample inhomogeneity, i.e., a row of voids along direction z, which are indicated in the upper thermography. In the lower part, the fit (full line) is arbitrarily extended over a larger region of the sample (circles) to obtain an effective value for the lateral thermal conductivity.

4. STATIONARY POINT-LIKE LASER HEATING

4.1. Analytical Treatment

Replacing the cylindrical lens in Fig. 2 with a spherical lens and appropriate focussing allow point-like laser heating of the sample (see

Fig. 9). If a disc-shaped sample of relatively small thickness ($D \ll R$) is used and heated on its axis, the resulting heat flow is radial, provided the thermal conductivity is isotropic within the disc plane. For a free-standing edge of the disc, the analytical solution for the stationary temperature increase is [15]

$$\Delta T(r) = C\,[K_1(R/l_0)\; I_0(r/l_0) + K_0(r/l_0)\; I_1(R/l_0)] \xrightarrow{l_0 \ll L} C_0\, K_0\left(-\frac{r}{l_0}\right). \tag{4}$$

Here l_0 denotes the same decay length as for the line-shaped focussing (see Eq. 2). K_n denotes the modified Bessel-function of the second kind and nth order, I_n is the modified Bessel function of the first kind and nth order, and C is a constant, which depends on the power input. The prefactor (C) and the decay length l_0 are fitted for evaluation of measured temperature profiles. The latter yields the lateral thermal conductivity as in the case of line-wise laser focussing. The limiting case of negligible edge effects is also included in Eq. (4), but is only valid for a steep temperature gradient next to the focus.

4.2. Experimental Results

Measurements with disc-shaped samples and appropriate point-like heating are shown and compared in Fig. 10. For the parallel fiber orientation, the broader temperature distribution and the lower peak temperature are obvious when compared to the thermography picture for the perpendicular fiber orientation. This is the same qualitative behavior as in the case of line-wise heating. With perpendicular fiber orientation and vertical arrangement of the fiber mats, a distortion of the isotherms next to the focus can be observed, indicating an anisotropy of the thermal conductivity within the disc plane (see Fig. 10, top right). A quantitative evaluation of the ellipsoidal temperature distortion was not applied due to the mismatch with respect to the boundary conditions involved in the derivation of Eq. (4).

Even for the parallel fiber orientation the radial symmetry is not perfect, as indicated by the difference between vertical and horizontal temperature profiles (see Fig. 10 bottom). This indicates material inhomogeneities or an influence of the fixation at the right edge. Nevertheless, the data derived from radial averaging of the temperature distribution are in agreement with Eq. (4). The fit yields an effective value for the lateral thermal conductivity of $\lambda_{II} = (0.79 \pm 0.08)\,\mathrm{W \cdot m^{-1} \cdot K^{-1}}$. The uncertainty is increased compared to the line focus case due to the imperfect shape of the sample edge. The described asymmetry of

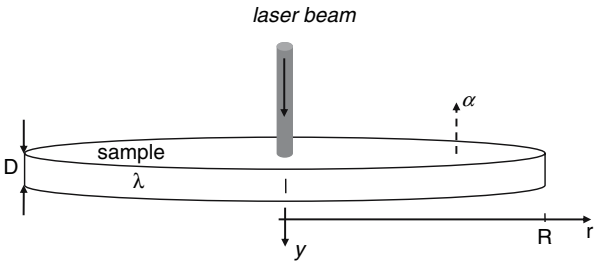

Fig. 9. Schematic diagram of the disc-like sample and the point-shaped laser beam, analogous to Fig. 4.

different radial temperature profiles correspond to a variation in λ_{II} of about 10%. Nevertheless, the obtained value agrees with the fore-mentioned result for line-wise heating.

5. PERIODIC LINE-WISE HEATING

5.1. Analytical Treatment

The evaluation of the dynamic measurement is based on the one-dimensional heat conduction equation, taking surface heat losses into account and neglecting edge effects. In the following, only the oscillatory part is considered, which is superimposed on the stationary temperature profile $\Delta T(x)$, caused by the (time-averaged) mean power input of the laser:

$$T(x,t) = T_0 + \Delta T(x) + \delta T(x) e^{i\omega t}. \tag{5}$$

In Eq. (5), T_0 denotes the constant temperature of the surroundings and the stationary temperature increase $\Delta T(x)$ is given by Eq. (1). The third term in Eq. (5) represents the temperature oscillation under quasi-stationary conditions with the heating angular frequency ω and the complex pre-factor $\delta T(x)$. The latter can be derived for the boundary conditions under consideration [13,17] as

$$\delta T(x) \propto e^{\left(-\sqrt{\frac{i\omega\rho c_p + 2\alpha/D}{\lambda}}|x|\right)} \tag{6}$$

where ρ is the sample density and c_p is the specific heat capacity; the other quantities are defined the same as in Eq. (2). The spatial variation of the thermal wave can be expressed separately for the amplitude;

$$|\delta T(x)| = \delta T_0 \, e^{-|x|/l_a} \tag{7}$$

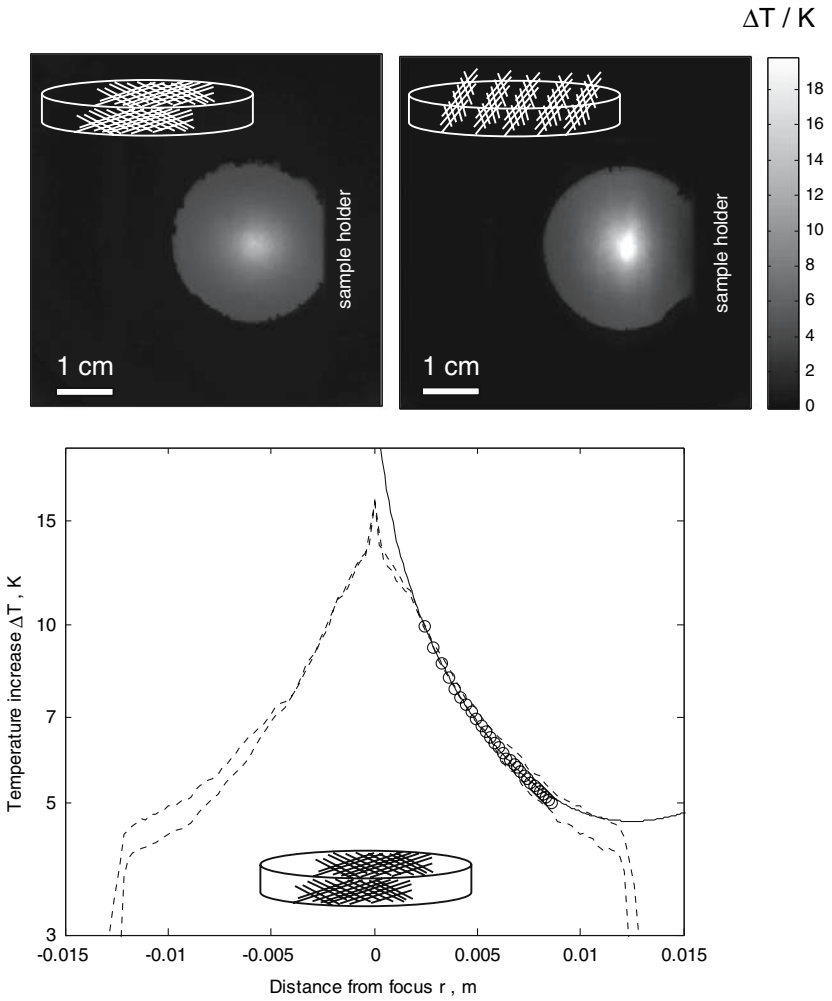

Fig. 10. Experimental results for disc-shaped samples of different fiber orientation in a representation analogous to Fig. 7. Samples are fixed at their right edge. Only for the case of parallel fiber orientation (top left), the evaluation with respect to the radial distance r is performed (lower part). Here single profiles in vertical and in horizontal directions are shown as dashed lines. The evaluated region, which was radially averaged in the free-standing half, is depicted as circles, the corresponding fit (Eq. 4) as full line.

and the phase is

$$\phi(x) = \arg[\delta T(x)] = -|x| / l_{\mathrm{p}} + \phi_0 \tag{8}$$

by rearranging Eq. (6) [13] with ϕ_0 as a constant phase shift. In Eqs. (7) and (8), the spatial variation is given in terms of a thermal diffusion length for the amplitude l_a and for the phase l_p. Using these diffusion lengths l_a and l_p, the thermal diffusivity $a = \lambda/(\rho c_p)$ can be estimated from the amplitude or the phase of the thermal wave according to $a_a = l_a^2\omega/2$ or $a_p = l_p^2\omega/2$ [18]. In general, these two quantities differ for the case of surface heat losses, i.e., $a_p > a_a$. It can be derived from the detailed analytical solution that the geometric mean of these two (apparent) thermal diffusivities is independent of surface heat losses [13,17]. The geometric mean a, representing the "true" value, is given as

$$a = \lambda/(\rho c_p) = \sqrt{a_a a_p} = l_a l_p \omega/2. \tag{9}$$

The effect of heat losses is influenced by the heating frequency, which is an independent measurement parameter to test the validity of Eq. (9) [13]. As for the stationary method, only the spatial variation of the thermal wave, i.e., the quantities l_a and l_p, are used for evaluation together with the heating frequency $f = \omega/(2\pi)$.

5.2. Experimental Results

The periodic heating was realized by modulating the output of the laser diode and the recording of a series of 126 pictures by the thermography system. The data acquisition was started without triggering after some minutes of periodic heating, which is necessary to reduce the effect of transients. The time interval for acquisition of IR-pictures was adapted to the heating frequency, in order to acquire at least three full time periods of oscillation. For further data evaluation a "zero picture" with equivalent stationary heating was subtracted from the acquired series of IR-pictures, in order to separate the oscillatory temperature signal. As in the stationary case, the temperature was extracted from the thermography by vertical averaging for each time step and lateral position. The temperature history of each lateral position was fitted to a sinusoidal curve yielding the amplitude and phase (with respect to the arbitrarily chosen phase in the focus position). As clearly shown in Fig. 11, the lateral region for further evaluation was restricted by the disturbing effects of multi-dimensional heat flow in the focus region and by the decrease of the temperature signal for larger distances from the heating laser. The fit of the phase and the amplitude to Eqs. (8) and (7), respectively, exhibited good agreement between measured data and the correlation, yielding the decay length for both the phase and amplitude (Fig. 12).

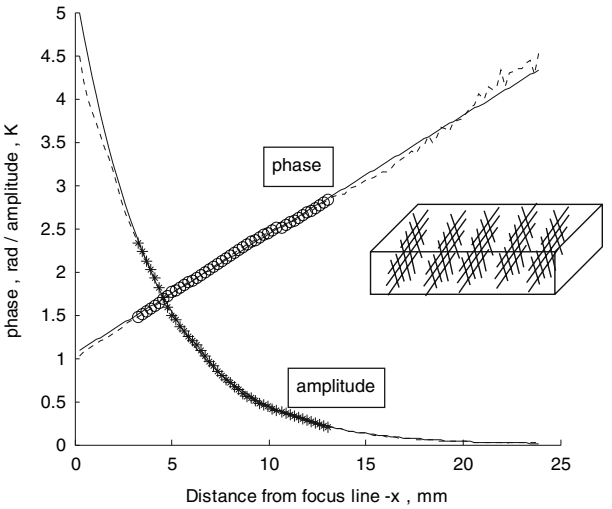

Fig. 11. Results derived from a single dynamic experiment with periodic line-wise heating at a frequency of 0.025 Hz for the sample with perpendicular fiber orientation. Both phase (circles) and amplitude (crosses) are depicted as a function of the lateral distance from the focus line. Data for the whole lateral range are represented by dotted line, values used for evaluation by symbols and the corresponding fit by a full line.

The decay lengths were used for calculation of the apparent thermal diffusivities a_a (amplitude) and a_p (phase) and their geometric mean (a). As shown in Fig. 12, the difference between a_a and a_p is largest for smaller frequencies, since the measurement approaches the stationary case. The difference decreases with increasing heating frequencies, since the oscillatory heat flow is dominated by effects of the heat capacity. On the other hand, the heating frequency is limited by the decrease of the measured temperature signal, i.e., the amplitude, which is responsible for the relatively large measurement uncertainty indicated by the error bars in Fig. 12. Nevertheless, the geometric mean thermal diffusivity is independent of the heating frequency, taking the uncertainty of the single data points into account. This is in agreement with Eq. (9) and is valid for measurements with both parallel and perpendicular fiber orientations. For the case of parallel fiber orientation, an influence of the fit results from the chosen spatial region was obtained, since the effect of multi-dimensional heat flow next to the focus is enhanced (see Sec. 3.2). This was taken into account by choosing larger distances ($-x$) for evaluation.

Resulting thermal diffusivities are $a_{II} = (3.9 \pm 0.4)\,mm^2 \cdot s^{-1}$ and $a_{\perp} = (2.22 \pm 0.15)\,mm^2 \cdot s^{-1}$ for the case of parallel and perpendicular fiber

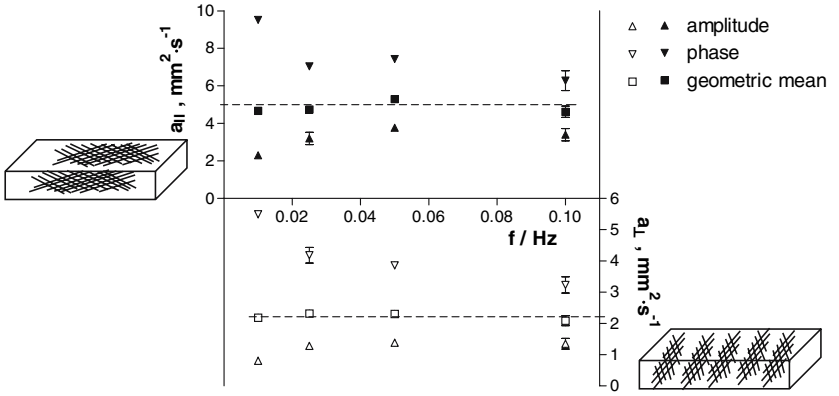

Fig. 12. Evaluation of the dynamical experiments for different heating frequencies (abscissa) for the parallel fiber orientation (top part, full symbols, left axis) and the perpendicular fiber orientation (bottom part, open symbols, right axis). The (apparent) thermal diffusivities, derived from the spatial variation of amplitude and phase, are depicted as triangles. Calculated geometric means, representing the "true" thermal diffusivities, are shown as squares, their averaged values as horizontal line. The depicted uncertainties are derived only from the uncertainty of the corresponding fit to Eq. (7) or Eq. (8).

orientations, respectively. The given uncertainty is estimated from the influence of the spatial evaluation region on the result. The uncertainty, which is enhanced for the case of parallel fiber orientation, is reflected in the scatter of the results for different heating frequencies, for which the spatial evaluation region had to be adapted. With the measured sample density ($\rho = 230\,\mathrm{kg \cdot m^{-3}}$) and a literature value for the specific heat capacity of carbon ($c_p = 800\,\mathrm{J \cdot kg^{-1} \cdot K^{-1}}$ [19]), the following thermal conductivities are calculated: $\lambda_{\mathrm{II}} = (0.89 \pm 0.09)\,\mathrm{W \cdot m^{-1} \cdot K^{-1}}$ and $\lambda_{\perp} = (0.41 \pm 0.03)\,\mathrm{W \cdot m^{-1} \cdot K^{-1}}$.

6. COMPARISON BETWEEN RESULTS FROM THERMOSCAN AND HOT-PLATE MEASUREMENTS

Besides the mentioned variations, additional tests were performed and summarized in Table I. An averaged value of thermal conductivity perpendicular to the fiber orientation was obtained by use of a guarded-hot-plate apparatus (GHP) with an imposed temperature difference of 10 K, i.e., temperature levels of 19°C and 29°C at the cold and hot plates, respectively. A relatively large sample with dimensions of ($1.1 \times 15 \times 15\,\mathrm{cm^3}$) was used, which was produced in a similar way as the samples used for the Thermoscan technique. The sample has a density of $\rho = 240\,\mathrm{kg \cdot m^{-3}}$.

The fiber-mats are orientated parallel to the surface of the tile. So, the GHP-apparatus imposed a heat flow perpendicular to the fiber-mats, yielding a spatially averaged value for the perpendicular thermal conductivity $\lambda_\perp$ [20].

For the Thermoscan technique, the dependence of the perpendicular thermal conductivity on the gas pressure (p) was tested by varying the gas pressure within the vacuum chamber. This is of interest for accuracy reasons and because the use of insulation material might be under normal gas pressure conditions. In addition, the results of the guarded-hot-plate measurement were obtained at ambient gas pressure and thus an estimate of the gaseous conductivity is needed to compare the results derived via the two different techniques. Hereby it has to be kept in mind that evaluation of the Thermoscan technique is based on the validity of Eq. (3), i.e., heat transfer from the sample surface to the surroundings must not be increased by gaseous conduction or even free convection. Based on tests with a (bulk) reference-sample without gas-pressure dependence, the applicability of the Thermoscan technique up to pressures of 30 mbar was confirmed. With the carbon-aerogel felt, a 20% increase of the component $\lambda_\perp$ was observed for $p = 30$ mbar. Thus, the influence of the presence of atmospheric gas on the thermal conductivity cannot be neglected at these gas pressures, in contrast to the case for a pure nanostructured aerogel. Within the long cracks of the composite under investigation, the gas conductivity increases at significantly lower gas pressures as in the small pores of the aerogel network. In the latter, an increase of the gas thermal conductivity is expected at gas pressures above about 100 mbar. Nevertheless, it can be also concluded for the composite that full gaseous conductivity is smaller than the contribution of solid thermal conductivity, which is measured in vacuum by the Thermoscan technique.

As shown in Table I, the results of different methods for the thermal conductivity parallel to the fiber-mats (λ_{II}) are in good agreement, taking into account the larger uncertainty for the value from the Thermoscan experiment with periodic heating. The results perpendicular to the fiber-mats ($\lambda_\perp$) scatter to some extent, which is probably due to material inhomogeneity. This is consistent with the fact that the spatially averaged value from the guarded-hot-plate measurement lies between the values obtained by the Thermoscan-method. The uncertainty of the guarded-hot-plate results is estimated to be about 12%. This large uncertainty is due to the relatively high thermal conductivity of the sample and possible thermal contact resistances between the sample and measuring plates, which can cause systematically lower λ-values.

Table I. Thermal Conductivities of the Carbon-Aerogel Felt under Investigation

Method (heating)	Gas pressure (mbar)	Orientation of the fibers with respect to heat flux	Thermal conductivity ($W \cdot m^{-1} \cdot K^{-1}$)
Thermoscan (stationary, line-wise)	$\approx 10^{-3}$	Parallel λ_{II}	0.76 ± 0.05
Thermoscan (periodic, line-wise)			0.89 ± 0.09
Thermoscan (stationary, point-like)			0.79 ± 0.08
Thermoscan (stationary, line-wise)	$\approx 10^{-3}$	Perpendicular $\lambda_{\perp}$	0.40 ± 0.03(>0.20)
Thermoscan (periodic, line-wise)			0.41 ± 0.03
Thermoscan (stationary, line-wise)	≈ 30		0.48 ± 0.03
Guarded-hot plate (GHP)	1013		0.34 ± 0.04

(Results were obtained at ambient conditions ($T \approx 25°C$) with different measurement techniques, conditions, and fiber orientation. For the Thermoscan results with perpendicular fiber orientation, the estimate of the lower limit is given in brackets.)

7. CONCLUSION

Using the Thermoscan technique, we succeeded in determining the thermal conductivity components of an anisotropic carbon aerogel-fiber composite both in stationary and in dynamical measurement variations. This technique allows the thermal characterization of relatively small samples, which are too small for a guarded-hot-plate measurement and too inhomogeneous for the laser-flash technique. The results of different methods for the thermal conductivity both parallel to the fiber mats (λ_{II}) and perpendicular to the fiber mats ($\lambda_{\perp}$) are in good agreement, taking material inhomogeniety into account (see Table I). As a result, the structural features of the carbon-aerogel-felt under investigation lead to a thermal anisotropy ratio of about two. This anisotropy is moderate, probably since the portion of the pinning-fiber bundles is substantial.

Additionally, preliminary tests were performed to determine the anisotropy in the electrical conductivity (σ), which should also be influenced by the microstructure and its anisotropy. A simple four-probe technique with copper plates as current leads and needles as voltage taps was applied to large samples with similar preparation parameters as the samples for thermal characterization. The felt without aerogel exhibited an anisotropy factor ($\sigma_{II}/\sigma_{\perp}$) of about 2.5, the aerogel-fiber compound of about 3.3. A relatively large measurement uncertainty of about 50% arose from the small resistance values, inhomogeneous structure, and the resulting scatter of the single measurement points. Nevertheless, the fact of

moderate anisotropy was confirmed in agreement with the thermal properties, indicating the essential influence of the pinning-fiber bundles.

ACKNOWLEDGMENT

We thank the "Bayerische Forschungsstiftung (BFS)," Munich, for financial support within the framework of the German joint project FORCARBON.

REFERENCES

1. R. W. Pekala and F. M. Kong, *Proc. 2nd Int. Symp. on Aerogels* (Montpellier, France, 1989), C4-34, C4-35.
2. J. Fricke and R. Petricevic, *Carbon Aerogels, Handbook of Porous Solids*, F. Schüth, K. Sing, and J. Weitkamp, eds. (Wiley-VCH, Weinheim, 2002), Vol. 3, pp. 2037–2062.
3. J. Fricke, *High. Temp.-High Press*. **25**:379 (1993).
4. W. J. Parker, J. R. Jenkins, P. C. Butler, and G. I. Abbott, *J. Appl. Phys*. **32**:1679 (1961).
5. S. O. Preston, *High. Temp.-High Press*. **27/28**:111 (1995/1996).
6. J.-C. Krapez, L. Spagnolo, M. Frieß, H.-P. Maier, and G. Neuer, *Int. J. Therm. Sci.* **43**:967 (2004).
7. G. Kalogiannakis, D. V. Hemelriejck, S. Longuemart, J. Ravi, A. Okasha, and C. Glorieux, *J. Appl. Phys.* **100**:063521 (2006).
8. J. Rantala, *Rev. Sci. Instrum.* **63**:5472 (1992).
9. V. Drach, H. P. Ebert, and J. Fricke, *Proc. 3rd Eur. Therm. Sci. Conf. 2000*, E. W. P. Hahne, W. Heidemann, and K. Spindler, eds. (Edizioni ETS, Pisa, 2000), Vol. 2, pp. 637–643.
10. V. Drach, H. P. Ebert, and J. Fricke, *High. Temp.-High Press* **32**:337 (2000).
11. R. Breiter, W. Cabanski, R. Koch, K.-H. Mauk, W. Rode, J. Ziegler, K. Eberhardt, R. Oelmaier, M. Walther, and H. Schneider, *Proc. Int. Conf. Infrared Sensors and Systems (IRS^2 2000)* (AMA Services, Wunsdorf, 2000), pp. 25–32.
12. V. Drach, G. Harhausen, H. P. Ebert, and J. Fricke, *Proc. Int. Conf. Infrared Sensors and Systems (IRS^2 2002)* (AMA Services, Wunsdorf, 2002), pp. 191–196.
13. A. Wolf, P. Pohl, and R. Brendel, *J. Appl. Phys*. **96**:6306 (2004).
14. H. S. Carslaw and J. C. Jaeger, *Conduction of Heat in Solids* (Clarendon Press, Oxford, 1959), Section. 4.6, p. 142.
15. H. S. Carslaw and J. C. Jaeger, *Conduction of Heat in Solids* (Clarendon Press, Oxford, 1959), Section. 4.6, p.143.
16. *HEAT2 Version 4.0*, http://www.blocon.se, http://www.buildingphysics.com
17. H. Altmann, *Bestimmung der Temperaturleitfähigkeit dünner Schichten mit dem Angström-Verfahren*, Ph. D. Thesis, University of Würzburg (1997).
18. H. S. Carslaw and J. C. Jaeger, *Conduction of Heat in Solids* (Clarendon Press, Oxford, 1959), p. 66.
19. Y. S. Touloukian, R. W. Powell, C. Y. Ho, and P. G. Klemens, *Thermophysical Properties of Matter*, Vol. 5, Specific Heat Capacity, Nonmetallic Solids (IFI/Plenum, New York, 1979), p. 9.
20. *DIN EN 12667*, Deutsches lustitut fur Normung e.v., Thermal performance of building materials and products—Determination of thermal resistance by means of guarded not plate and heat flow meter methods—products of high and medium thermal resistance; German version EN 12667:2001 (Beuth, Berlin).